

**SPARC-RF-11/005**  
**KEK Report 2011-6**

**1 September 2011**

**High Gradient Test of a C-Band Accelerating Structure Prototype  
for Energy Upgrade  
of Frascati Photoinjector SPARC**

D. Alesini, R. Boni, G. Di Pirro, R. Di Raddo, M. Ferrario, A. Gallo, V. Lollo, F. Marcellini,  
INFN-LNF, Frascati (Roma), Italy

L. Palumbo, V. Spizzo  
Sapienza-University of Rome & INFN-LNF, Italy

A. Enomoto, T. Higo, K. Kakihara, T. Kamitani, S. Matsumoto, T. Sugimura, K. Yokoyama,  
High Energy Accelerator Research Organization, KEK  
1-1 Oho, Tsukuba, Ibaraki 305-0801 Japan

S. Verdú-Andrés  
TERA Foundation, Novara, Italy  
Instituto de Física Corpuscular IFIC (CSIC-UV), Paterna (Valencia), Spain

***ABSTRACT***

*This report describes the activities carried out by the Frascati INFN Laboratories in close collaboration with the Japanese Laboratory KEK for the development and high-power RF test of a prototype of a room-temperature C-band travelling-wave accelerating structure. The results of the power test on the prototype should assist the choice of two accelerating structures aimed at increasing the energy of the S-band photoinjector SPARC, which is currently in operation at LNF.*

*From the experimental results, we confirmed the operation of the prototype at 50 MV/m with about  $10^6$  breakdowns per pulse per meter. This brings us to realize the actual sections following the technical choices adopted for the prototype. Maximum breakdowns were observed near the output coupler. This indicates the negative effect of the cutting and re-brazing stages before the final completion of the present test structure. However, this kind of intervention, necessary to eliminate some deformation of the structure occurred during the brazing process, will not be repeated with a more accurate production.*

# High-Gradient Test of C-Band Accelerating Structure Prototype for Energy Upgrade of Frascati Photoinjector SPARC

D. Alesini, R. Boni, G. Di Pirro, R. Di Raddo, M. Ferrario, A. Gallo, V. Lollo, F. Marcellini  
INFN-LNF, Frascati (Roma), Italy

L. Palumbo, V. Spizzo  
Sapienza-University of Rome & INFN-LNF, Italy

A. Enomoto, T. Higo, K. Kakihara, T. Kamitani, S. Matsumoto, T. Sugimura, K. Yokoyama,  
High Energy Accelerator Research Organization, KEK  
1-1 Oho, Tsukuba, Ibaraki 305-0801, Japan

S. Verdú-Andrés  
TERA Foundation, Novara, Italy  
Instituto de Física Corpuscular IFIC (CSIC-UV), Paterna (Valencia), Spain

## ABSTRACT

*This report describes the activities carried out by the Frascati INFN Laboratories in close collaboration with the Japanese Laboratory KEK for the development and high-power RF test of a prototype of a room-temperature C-band travelling-wave accelerating structure. The results of the power test on the prototype should assist the choice of two accelerating structures aimed at increasing the energy of the S-band photoinjector SPARC, which is currently in operation at LNF.*

*From the experimental results, we confirmed the operation of the prototype at 50 MV/m with about  $10^6$  breakdowns per pulse per meter. This brings us to realize the actual sections following the technical choices adopted for the prototype. Maximum breakdowns were observed near the output coupler. This indicates the negative effect of the cutting and re-brazing stages before the final completion of the present test structure. However, this kind of intervention, necessary to eliminate some deformation of the structure occurred during the brazing process, will not be repeated with a more accurate production.*

## 1 INTRODUCTION

To upgrade the beam energy of the photoinjector SPARC from 170 MeV to approximately 250 MeV, the LNF Accelerator Division decided to replace one 3-m-long low-gradient S-band travelling-wave (TW) accelerating section with two 1.4-m-long structures operating in the C-band (i.e., at 5712 MHz), as shown in Fig. 1-1.

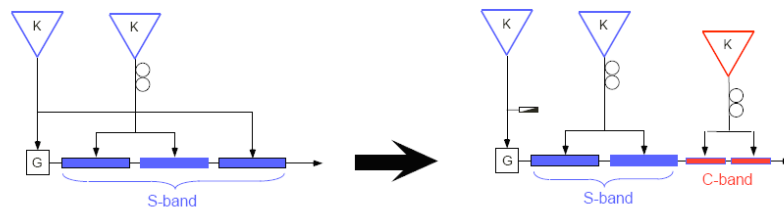


Fig. 1-1: Layout of SPARC with C-band system.

SPARC is a 150-MeV test facility used to produce high-brightness electron beams for driving SASE-FEL experiments in visible light and explore the most critical aspects of future X-ray source subsystems. The beam is generated by a 1.6-cell standing-wave RF gun and accelerated with three constant-gradient  $2\pi/3$  travelling-wave structures. Thus far, the SASE radiation [1] and the beam velocity bunching (VB) [2] have been successfully achieved. Other advanced beam dynamics experiments and the generation of upper radiation harmonics with the seeding technique [3] are in progress.

The main motivations for upgrading the SPARC energy are the shifting of the SASE radiation closer to the ultraviolet (UV) region and improving the seeding experiment. The choice of the C band instead of the S band was dictated by other considerations: the opportunity to achieve a higher accelerating gradient, enabled by the higher frequency; the opportunity to explore a C-band accelerator combined with an S-band injector that, at least from beam dynamics simulations [4], seems very promising in terms of achievable beam quality; and the opportunity to gain experience with a rather new RF technology, in light of further upgrades of the SPARC photoinjector.

The new C-band structures will be fed by a Toshiba ET37202 50-MW C-band klystron. The HV pulsed modulator and the 400-W solid-state driver for the klystron were manufactured by ScandiNova (Sweden) and Mitec Telecom (Canada), respectively, and have already been installed and power tested at LNF. The new C-band system will also include a pulse compressor (a SLED called SKIP) that is presently under development.

An important assumption to support the abovementioned upgrade is that an average acceleration field of more than 35 MV/m will be obtained. This would result in a total energy gain of more than 100 MeV within the two C-band sections. It was decided to develop the C-band structures in the Frascati laboratories with the support of local firms. In order to simplify the electromagnetic and mechanical design, we chose a constant impedance (CI) structure with large irises that limit the surface  $E$ -field and allow a larger pumping speed. Large irises also allow us to increase the group velocity and, consequently, feed the unit with shorter RF pulses over a short filling time.

It must be noted that with the use of pulse compressors (i.e., SLED or SKIP), the decay of the RF pulse amplitude along a CI structure is compensated for the exponential shape of the SLED pulse, resulting in a rather constant profile of the RF field along the accelerating section.

To verify the validity of these technical choices, a prototype consisting of 20 RF cells and having a total length of 50 cm was designed, built, and brazed at LNF with the support of Italian firms. The prototype, details of which are given below, has been high-power tested in Japan at KEK, the High Energy Accelerator Research Organization, where a power station of 50 MW at 5712 MHz is available. This was done within the framework of a collaboration established ad hoc between KEK and INFN.

KEK has long been studying the high-gradient performance of S-band, C-band, and X-band accelerator structures [5,6,7]. Within this series of experiments, the present study was undertaken for KEK to further evaluate the feasibility of high-gradient performance of C-band accelerator structure, which is now being adopted for the FEL accelerators.

This report presents not only the design and construction phases of the prototype but also the results of the high-power tests and the analysis of various important aspects of the high-gradient performance of the structure.

## 2 STRUCTURE DESIGN

The design criteria of the C-band structures are shown and discussed in [8]. The structures are travelling-wave constant-impedance sections with symmetric axial input couplers and have been optimized to function with a SLED RF input pulse. The choice of a constant-impedance structure was made partly to reduce the fabrication costs but mainly to obtain a quasi-uniform accelerating field along the structure when the structure is fed by the SLED input.

The dimensions and shape of the single cell were optimized to obtain the following:

- a) the lowest peak electric field on the iris surfaces with the SLED input pulse;
- b) an average accelerating field of (at least) 35 MV/m with the power available from the klystron; and

- c) the largest possible iris aperture, compatible with the points above, in order to increase the pumping speed and thereby reduce the wake field contribution as well as the filling time of the structure itself.

A short filling time reduces the input pulse length and, therefore, the breakdown probability [9].

Figure 2-1 shows the final single-cell profile and the main dimensions, and Table 1 lists the final single-cell parameters for both the prototype and the final structure obtained by HFSS simulations [10].

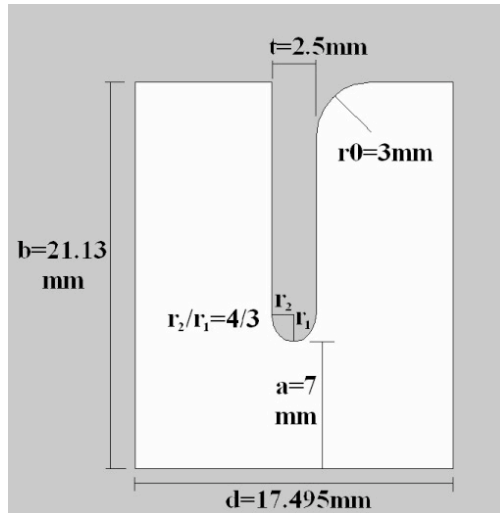


Fig. 2-1: Final dimensions of single cell.

The input and output couplers adopted are of the so-called waveguide coupler type. This type of coupler allows us to simultaneously obtain low pulsed heating [11,12] and compact symmetric feeding. The final mechanical drawing of the prototype is shown in Fig. 2-2. The input coupler includes a splitter, and the output coupler has two symmetric ports to connect to two RF loads. This reduces the dissipated RF power per load and the cost of the unit.

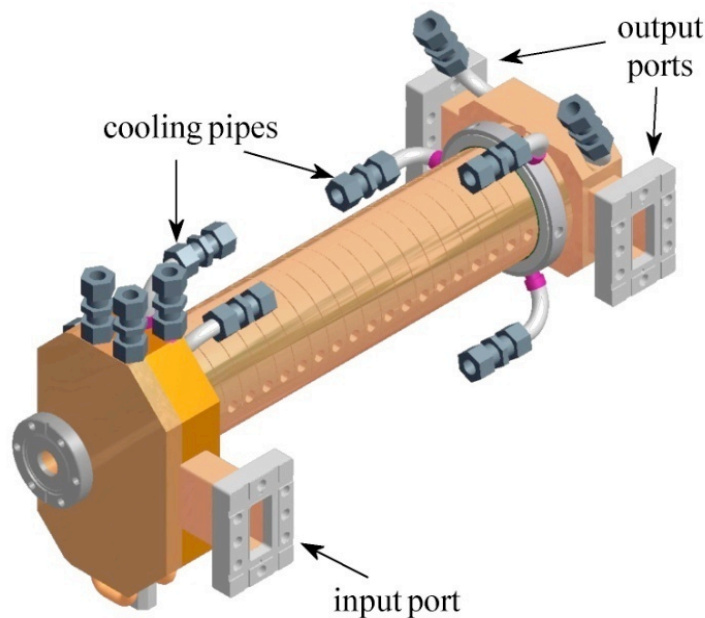


Fig 2-2: Mechanical drawing of prototype.

Table 1: Parameters of C-band structure

Parameter	Prototype	Final structure
Frequency ( $f_{RF}$ )	5.712 [GHz]	
Phase advance per cell	$2\pi/3$	
Number of accelerating cells ( $N$ )	22	71
Structure length including couplers ( $L$ )	0.54 [m]	1.4 [m]
Group velocity ( $v_g/c$ ):	0.0283	
Field attenuation ( $\alpha$ )	0.206 [1/m]	
Series impedance ( $Z$ )	34.1 [ $M\Omega/m^2$ ]	
Shunt impedance ( $r$ )	82.9 [ $M\Omega/m$ ]	
Filling time ( $\tau_F$ )	50 [ns]	150 [ns]
Power flow at $E_{acc} = 35$ MV/m	36 [MW]	
$E_{s\ peak}/E_{acc}$	2.17	
$H_{s\ peak}$ at $E_{acc} = 35$ MV/m	87.2 [kA/m]	
Pulsed heating at $E_{acc} = 35$ MV/m	<1 °C	
Average accelerating field with SLED input pulse after one filling time	60.2 [MV/m]	51.6 [MV/m]
Max peak surface field at the beginning of the SLED pulse with 120 MW peak SLED power	140 [MV/m]	
Energy gain (maximum and at 35 MV/m)	23.2 (13.5) [MeV]	64.1 (42) [MeV]
Output power	$0.85 \cdot P_{IN}$	$0.60 \cdot P_{IN}$
Average dissipated power at 10 Hz with SLED pulse length equal to one filling time	7.6 [W]	59.6 [W]

### 3 STRUCTURE FABRICATION

A photograph of a single cell is shown in Fig. 3-1(a). Each cell was machined as a cup to include a single iris. The integrated cooling system employs six longitudinal cooling pipes. Three tuners are inserted at  $120^\circ$  to one another, and these deform the outer wall of each cell in both directions. Cells were machined by a local firm [13] using a high-precision turning machine. The obtained surface roughness was less than 50 nm, and the precision in the dimensions was  $\pm 2\mu\text{m}$ .

The input coupler was fabricated by milling a single copper ingot with a computer-controlled machine and then was closed with a blanking plate brazed onto the coupler itself, together with the input flange. The obtained surface roughness was less than 200 nm, and the precision in all the dimensions was  $\pm 10\mu\text{m}$ . A photograph of the input coupler is shown in Fig. 3-1(b).

Before the brazing of the cells, they were cleaned with a detergent (ALMECO-19) and a mixture of organic (citric) acid and distilled water, in a bath with an ultra-sound machine.

To minimize the number of brazing processes and increase the speed of manufacturing, the inner surface of both rectangular output couplers was prepared by the electric discharge machining (EDM) technique. However, the coupling irises and the pipe were fabricated using a CNC milling machine. The obtained surface roughness of the waveguide was  $0.6\mu\text{m}$ , and the precision in the dimensions was  $\pm 20\mu\text{m}$ . A photograph of the output coupler is shown in Fig. 3-1(c).

The structure was brazed at LNF in a vacuum furnace through various steps. We brazed the couplers with all flanges and separately brazed the TW cells. Finally, the column of cells was positioned vertically in the vacuum furnace and brazed to the couplers with the input coupler placed at the bottom (Fig. 3-1(d)). The procedure was successful and vacuum tightness was obtained, but we discovered that the output coupler had a small angular tilt with respect to the main axis of the cell column. Therefore, a cut was necessary at the second cell from the output coupler. The joint surface of the main body column was re-machined, cleaned, and brazed again with the same BAg-8 brazing material to form the full body.

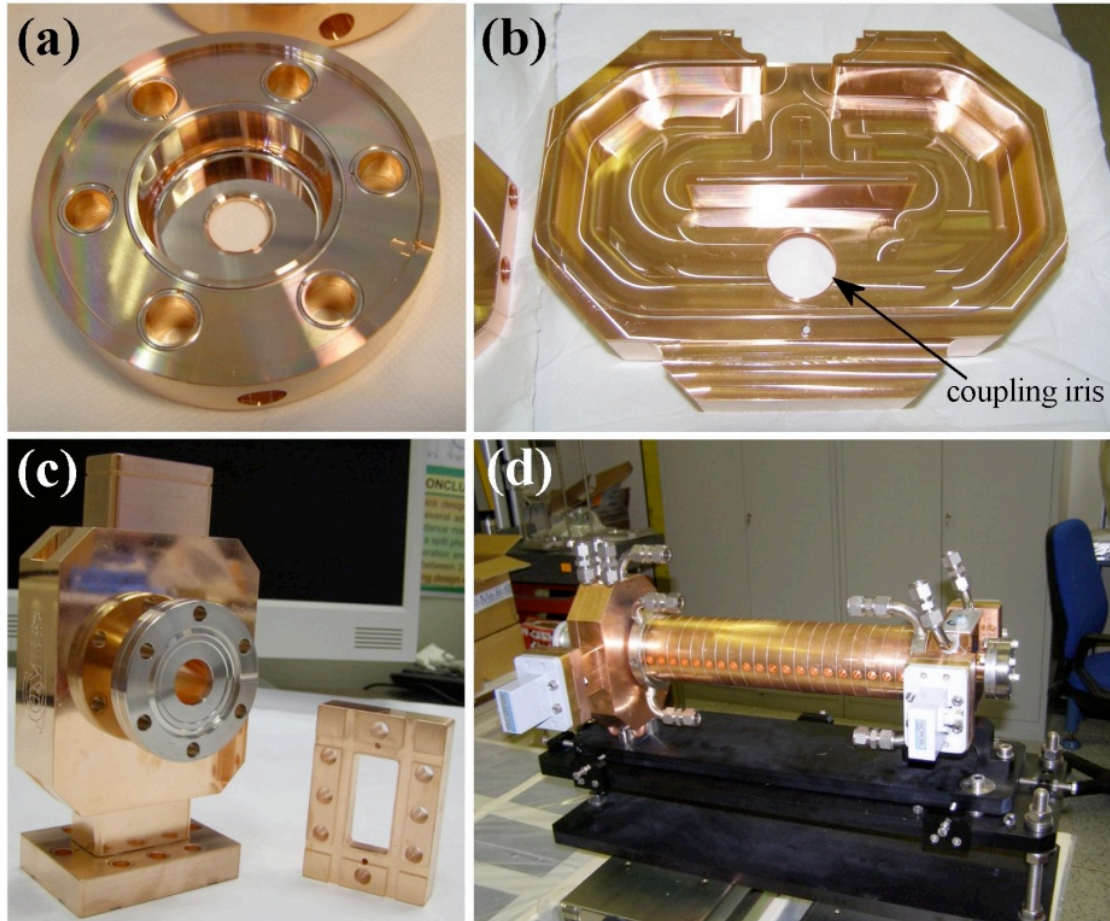


Fig. 3-1: (a) Regular cell; (b) input coupler; (c) output coupler; and (d) final prototype.

#### 4 LOW-POWER RF TEST

RF measurements were conducted at each brazing step and after the final brazing process. Figure 4-1 shows the scattering parameters after the final brazing (port 1 is the input port, and ports 2 and 3 are the output ports).  $S_{11}$  expected from the HFSS simulations was less than 0.01, whereas the measured value was 0.078. The expected  $S_{21}$  and  $S_{31}$  values were 0.647, whereas the measured values were 0.641 and 0.648, respectively.

We also measured the longitudinal electric field along the structure (using the bead-pull technique), and the result is shown in Fig. 4-2. The flat-top field undulation was about  $\pm 10\%$ . A ripple with a three-cell periodicity is evident, indicating a large reflection from the output coupler region. We were confident in our ability to compensate for this reflection by final tuning, but time did not permit that so we proceeded to the experiment without final tuning. In addition, we noticed that the main body cells and the output coupler were slightly misaligned, but this should not have been a concern in the high-power test.

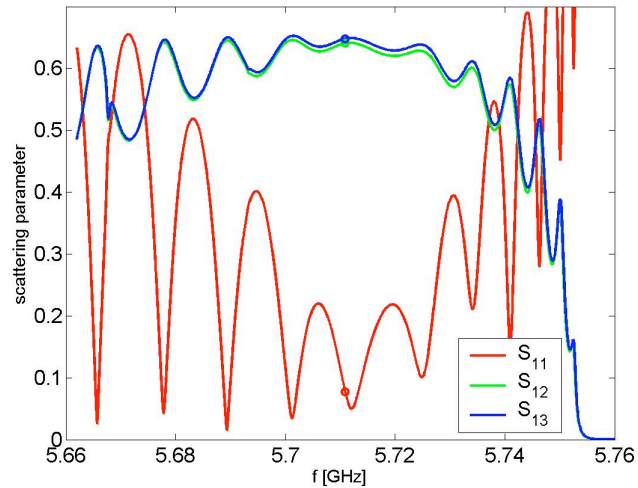


Fig. 4-1: Scattering parameters after final brazing (port 1 is the input port, and ports 2 and 3 are the output ports).

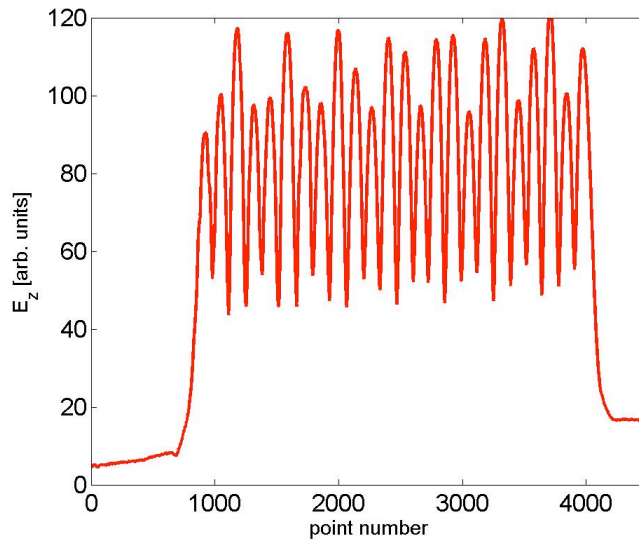


Fig. 4-2: Electric field profile of final brazed structure, as measured by bead-pull technique.

## 5 PREPARATION FOR HIGH-POWER TEST

### 5.1 High-power test system

A schematic of the complete system for the high-power test is shown in Fig. 5-1. The system consists of the following components: a klystron driven by a PFN modulator, the 22-m-long transport line of a circular low-loss waveguide in  $TE_{01}$  mode, a SLED-type pulse compressor called SKIP [14], and the test area of a vault with radiation shielding mostly provided by 50-cm concrete blocks.

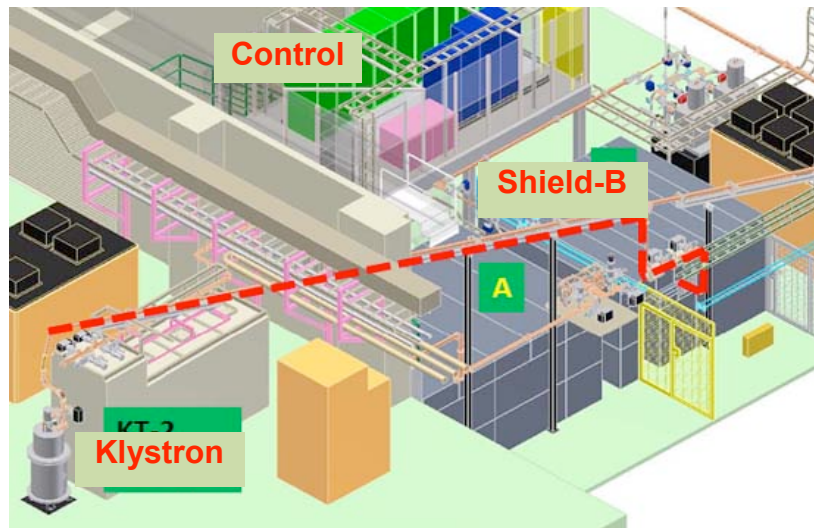


Fig. 5-1: General layout of test system. The RF power was produced by a C-band klystron and transported through a low-loss waveguide into a concrete vault (Shield-B).

### 5.2 Setup in concrete vault

The power distribution in the radiation-shielded room is shown in Fig. 5-2(a), and its schematic is shown in Fig. 5-2(b). The power from the klystron is transported by a low-loss waveguide to the roof of the concrete vault. It is converted to the  $TE_{10}$  mode by the rectangular waveguide and then admitted into the shielded room. The power is pulse compressed by SKIP, when needed, before feeding the accelerator structure. The on and off switching of SKIP is performed by the detuner rods shown in Fig. 5-2(c).

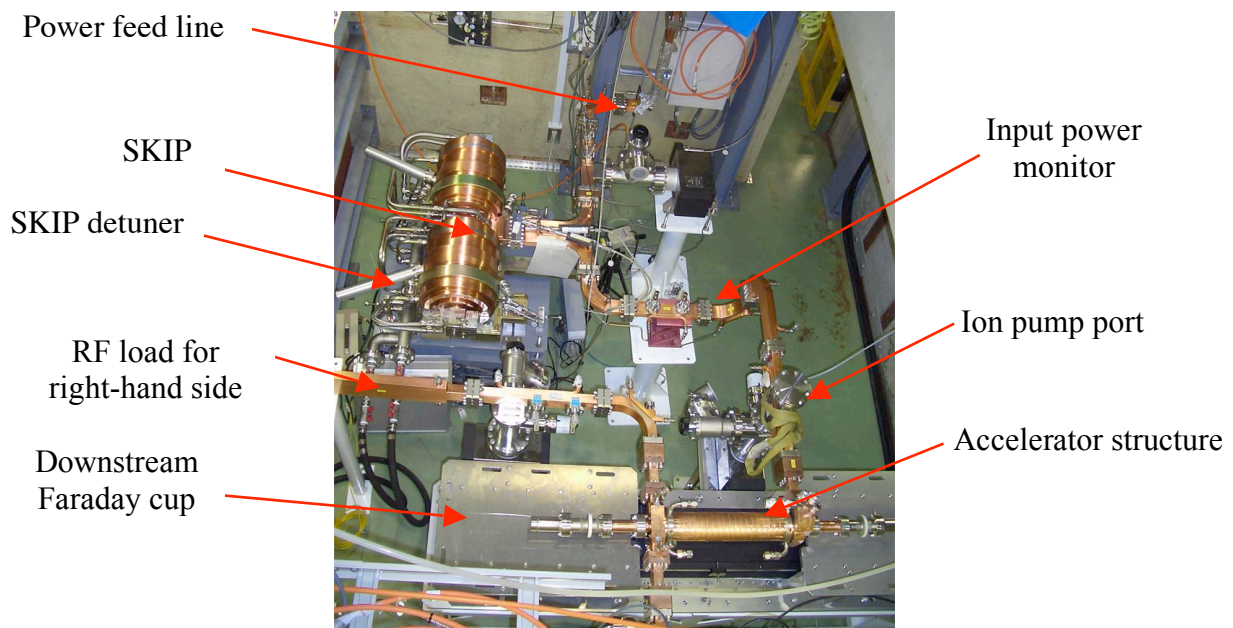


Fig. 5-2(a): Experimental setup inside shielded room.

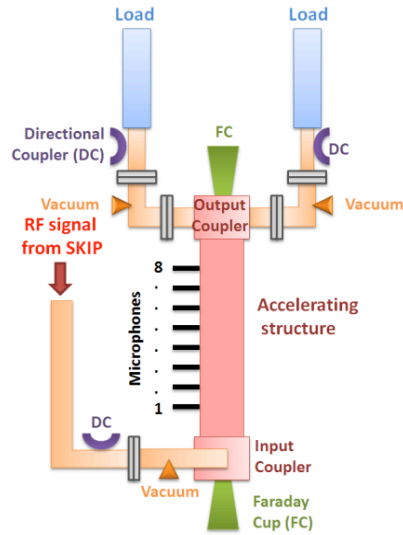


Fig. 5-2(b): Schematic of setup around accelerator structure [see ref. 15].

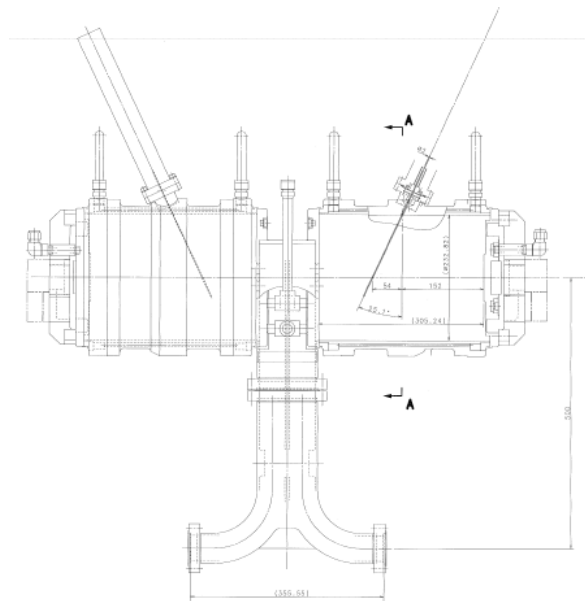


Fig. 5-2(c): SKIP detuning system.

### 5.3 Setup of test accelerator

The setup of the accelerator test structure is shown in Fig. 5-3. Evacuation was performed by ion pumps through waveguide evacuation ports, one in front of the input coupler and two in the output waveguides between the accelerator structure and RF loads. The input power was monitored by the directional coupler located between SKIP and the accelerator structure. The transmitted power was monitored in front of each RF load.

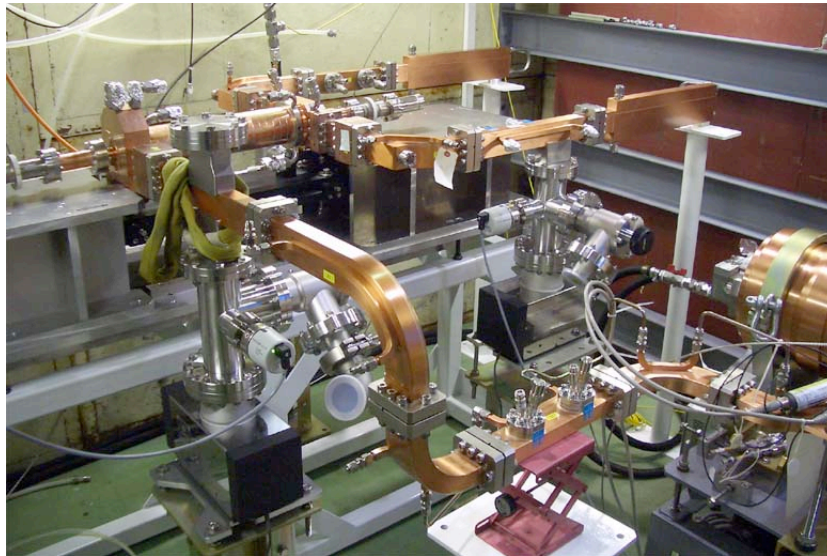


Fig. 5-3: Setup of accelerator test structure.

#### **5.4 Waveguide flanges**

There are many types of waveguide flanges. KEK has used the Merdinian type, the A-DESY (advanced-DESY) type, and the MO type[16]. During the early discussion on which type should be used, we decided to consider any reasonable selection that met the requirements for each existing component. Since the accelerator structure was newly fabricated, we had the freedom of any choice. We chose the A-DESY type, which was found almost the same as the DESY type. The components connecting to the test structure were made for the Merdinian type, so we used the conversion blocks seen in Fig. 5-3.

#### **5.5 Waveguide components**

We noticed a deterioration of the interior surface of the waveguides made by INFN for converting the flange types. By visual inspection, we suspected that the oxidization might cause poor high-power performance. Because these parts were attached to the test structure, we decided to treat them in a high-temperature hydrogen furnace. They were heated to higher than 600°C for 1 h in H<sub>2</sub> gas at atmospheric pressure. The discoloration pattern vanished, indicating the proper deoxidization. This process is shown by the photographs in Fig. 5-4.

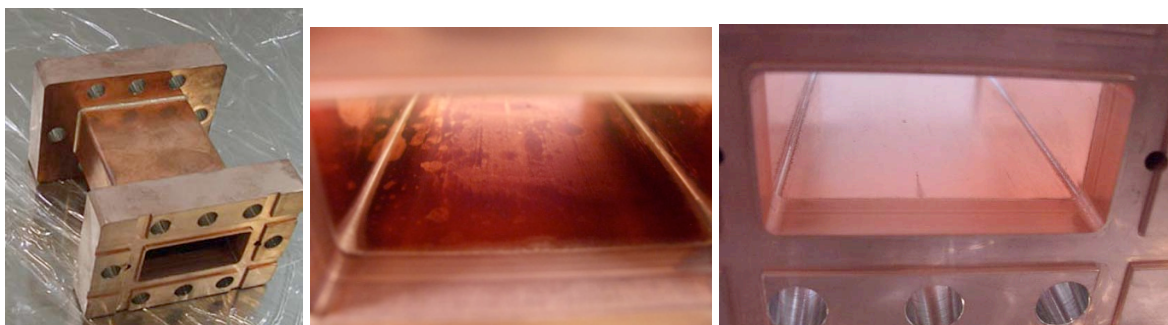


Fig. 5-4: Hydrogen furnace treatment of waveguides for flange adaptation.

## 5.6 SKIP pulse compressor

The pulse compression was performed by the SuperKEKB injector pulse compressor (SKIP) [14] shown in Fig. 5-2. This uses the  $TE_{0,3,8}$  mode at measured Q values of greater than 130,000. With flipping of the input RF phase for the final 0.35  $\mu\text{s}$  during the full 2- $\mu\text{s}$  RF pulse, an input power of 43 MW was found to have been compressed into an output power of 200 MW, confirming the power gain by a factor of about five.

## 5.7 RF dry load

The RF loads used in this experiment are shown in Fig. 5-2 [17]. These were designed to accept the RF power through a series of SiC buttons cooled indirectly by a copper wall in the H-plane of the rectangular waveguide. The pair was high-power tested up to half of the SKIP output power when driven by a klystron, meaning 100 MW per RF load for a few 100-ns pulses at 50Hz.

## 5.8 Power calibration

The RF power was monitored by a peak power meter (Gigatronics 8542B) and crystal sensors (typically Agilent 8473B). The most basic power estimation was performed with the former at the stage before installation of the accelerator structure and with SKIP detuned. The RF peak power was also measured and checked by the calorimetric method, from the temperature change in the cooling water of the RF dummy loads. The RF power was measured at each  $E_S$  level, with a set value of the PFN modulator voltage. Since the driving power for the klystron input cavity was maintained at the saturation level, the nominal output power level could be estimated from the  $E_S$  value.

Figure 5-5 shows the relation between the voltage  $E_S$  applied to the klystron and the power  $P_F$  delivered by the klystron. Figure 5-6 shows the relation between the power  $P_F$  delivered by the klystron and the accelerating gradient  $E_0$  achieved in the 0.35-m-long Frascati C-band test structure.

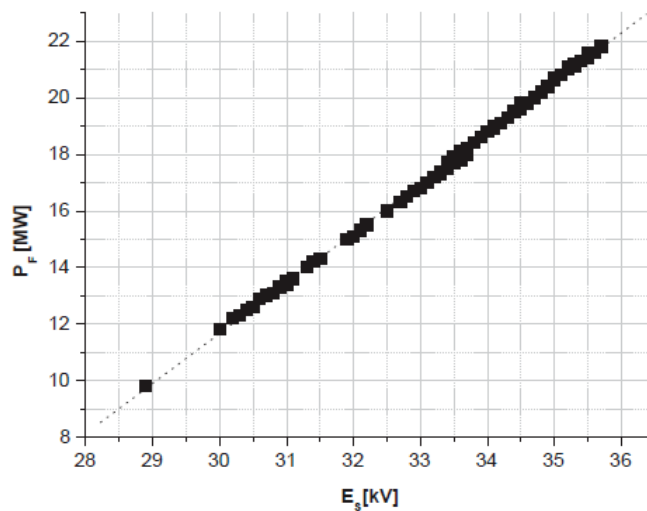


Fig. 5-5: Relation between voltage  $E_S$  applied to klystron and power  $P_F$  delivered by klystron.

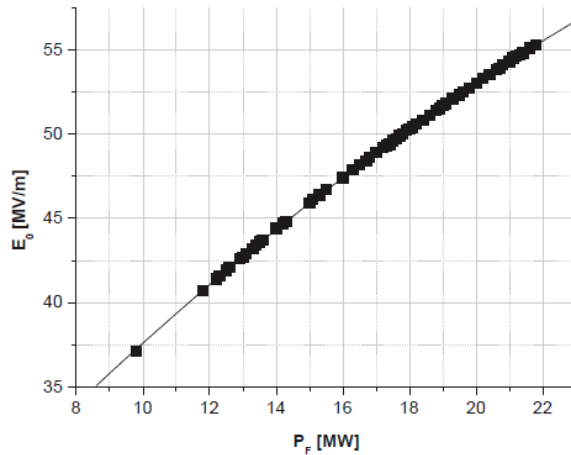


Fig. 5-6: Relation between power  $P_F$  delivered by klystron and accelerating gradient  $E_0$  in 0.35-m-long C-band test structure.

The SKIP power multiplication was estimated as follows: With SKIP detuned, a crystal diode was calibrated using a Tektronix digital scope in the range 2.5–30 MW. Next, a calibrated attenuator of 6.035 dB was inserted into the cable path between the waveguide monitor and the crystal diode to avoid its saturation. Then, by turning on SKIP, a power gain of 5.2 was measured.

### 5.9 Cooling of structure

Since persistent leaks were found in all three water channels intended for the body cooling of the accelerator structure, we decided to cool only the coupler regions in the early stage of the test. Later, and only for test purposes, we cooled the body portion with an independent cooling system with a reduced pressure. Then, the breakdown rate for a different body temperature was also measured.

### 5.10 Vacuum evacuation and its monitoring

The evacuation was done entirely through waveguide ports by ion pumps. The vacuum monitors were cold cathode gauges and all were located at the heads of these evacuation ports.

### 5.11 Acoustic sensors

Acoustic sensors were mounted on the test structure and various parts of the waveguide. Each sensor was a Keyence precision vibration sensor GH-313A with amplifier GA-245. This model has a sensitivity of  $-3$  dB in the frequency range from 40 Hz to 8 kHz. These were pressed against the surfaces by using fasteners as shown in Fig. 5-7.

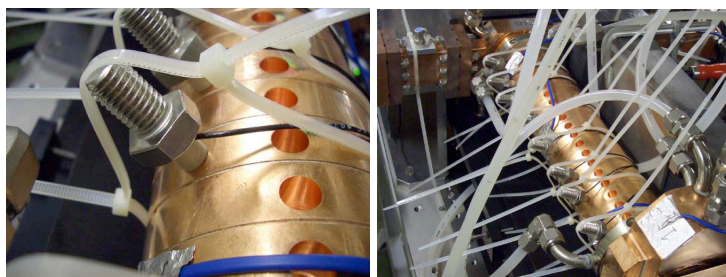


Fig. 5-7: Acoustic sensors mounted on test structure and on waveguide.

### 5.12 Dark current monitoring

The currents emitted from the accelerator structure were monitored in both directions. Pipes with an inner diameter of 40 mm were connected from the beam ports of the accelerator structure with ceramic insulation in front of the Faraday cups shown in Fig. 5-2. The stable currents were measured with a Keithley 6485-J picoammeter.

### 5.13 Radiation monitoring

The radiation level was monitored from time to time during the test period. This was carried out with an integration type of survey monitor.

## 6 PROCESSING HISTORY

The high-power test started on November 5 and was completed on December 13, 2010. For almost one month of processing, from November 5 until December 2, more than  $10^8$  RF pulses of 200-ns width were sent into the structure with a repetition rate of 50 Hz. For a couple of days the RF pulse length was changed to 300 ns and for one day (November 12) the repetition rate was decreased to 25 Hz. On November 15, SKIP was switched on. After that, the power  $P_{IN}$  into the structure was about five times the power  $P_F$  delivered by the klystron. Below are listed some of the relevant operational changes, and in Fig. 6-1 the full test history is shown in terms of the klystron output power  $P_K$  (equivalent to  $P_F$ ). The evolution of the test structure processing from November 22 until December 2 is shown in Fig. 6-2. Figure 6-3 shows the accelerating gradient reached and the breakdown rate versus the accumulated number of breakdowns.

The full history of the test structure processing was as follows:

November 5	Start high-power test of structure with 200-ns pulses at 50 Hz.
November 12	Change to operation at 25 Hz for one day.
November 15	Switch on SKIP.
December 13	Finish high-power test.

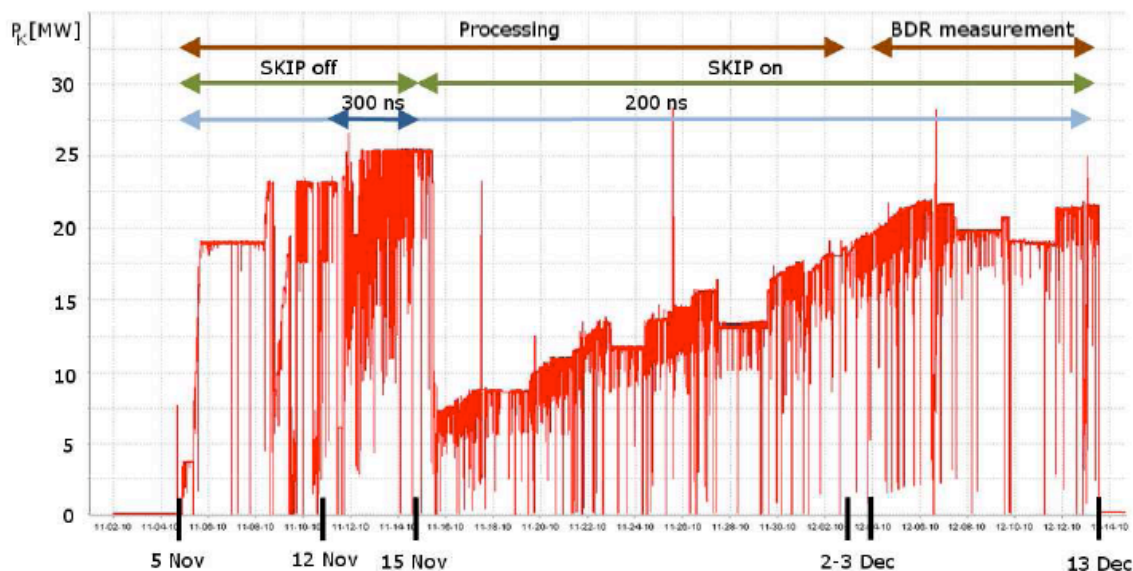


Fig. 6-1: History of high-power test of structure.

The klystron output power is along the vertical axis and the time is along the horizontal axis.

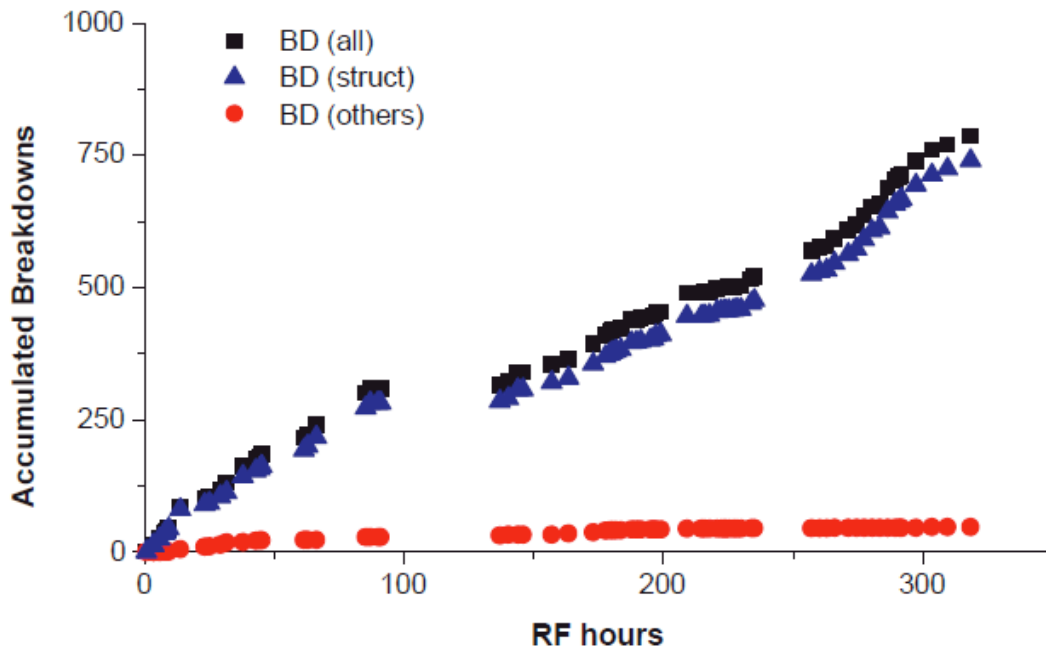


Fig. 6-2: Evolution of test structure processing from November 22 until December 2. Blue triangles represent breakdowns that occurred within the structure. Red circles represent breakdowns that occurred somewhere else in the RF circuit. Black squares represent the total number of breakdowns.

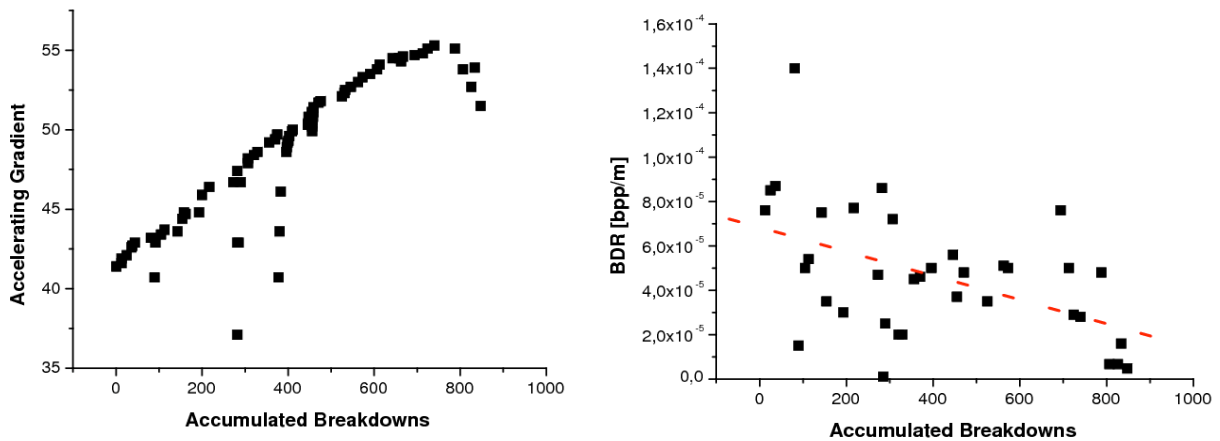


Fig. 6-3: Accelerating gradient and breakdown rate versus accumulated breakdowns.

## 7 VARIOUS HIGH-GRADIENT FEATURES

### 7.1 Typical breakdown pulse

The typical RF pulse shapes around the accelerator structure are shown in Fig. 7-1.

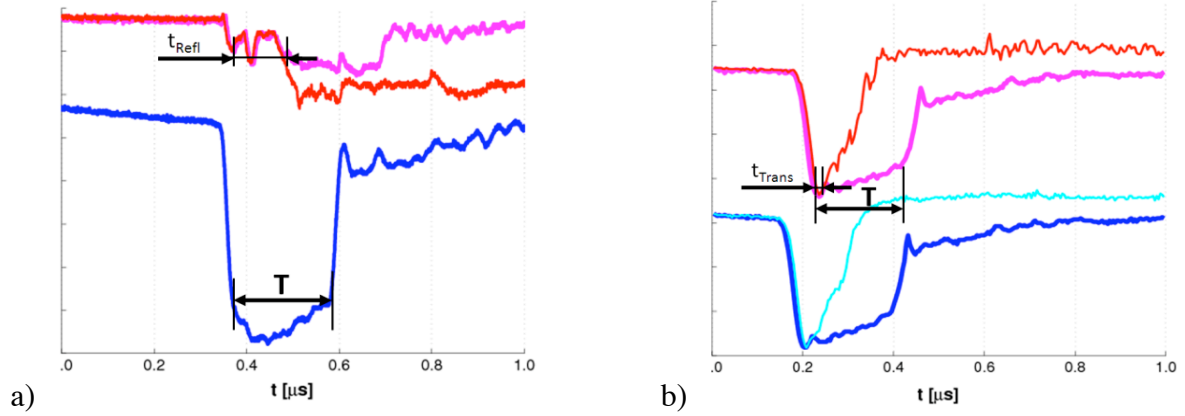


Fig. 7-1: Typical RF pulse shapes of breakdown: (a) RF pulse forward into accelerator structure (blue) and reflected from it (pink) during normal operation, and RF pulse reflected from accelerator structure during breakdown (red); (b) RF pulse transmitted through structure toward left RF load (pink) and right (blue) during normal operation, and RF pulse transmitted toward left RF load (red) and right (cyan) during breakdown.

## 7.2 Field emission measurements

The stable dark current was measured on December 3 for different field values and RF pulse lengths. Figure 7-2 shows the typical dark current signal monitored during normal operation (no RF breakdown) by the downstream Faraday cup (pink curve) together with the pulse transmitted from SKIP to the accelerating structure (blue curve).

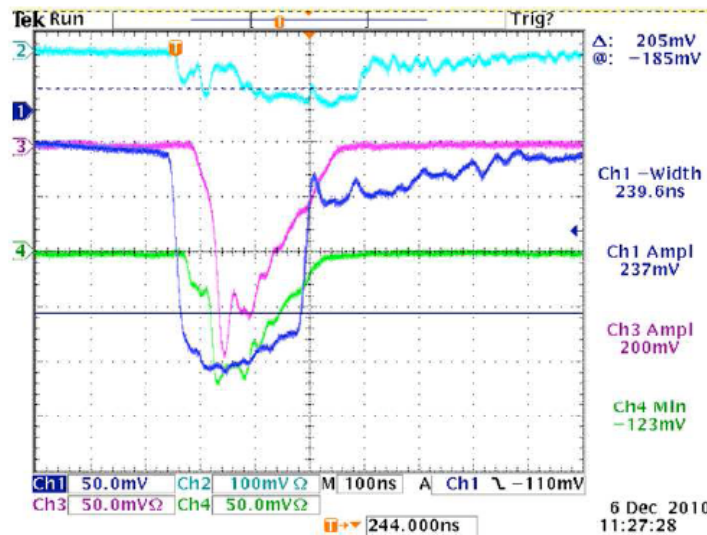


Fig. 7-2: Pulse shapes related to dark current during normal operation (no RF breakdown): Ch1 transmitted pulse from SKIP (blue curve), Ch2 reflected power to SKIP (cyan curve), Ch3 dark current from downstream Faraday cup (pink curve), and Ch4 dark current from upstream Faraday cup (green curve).

## 7.3 Dependence of dark current on peak surface electric field

The measurements were taken starting with the highest field value. The dependence of the dark current on the peak surface electric field  $E$  is shown in Fig. 7-3. The dark current from the upstream Faraday cup does not reproduce the Fowler-Nordheim behavior well. The field enhancement factor  $\beta$  can be obtained from the fitted slope (see [18]). The value of  $\beta$  is

approximately 90 for the Frascati C-band test structure. This was estimated from the dark current measured in the downstream Faraday cup, taking the work function of copper as 4.5 eV.

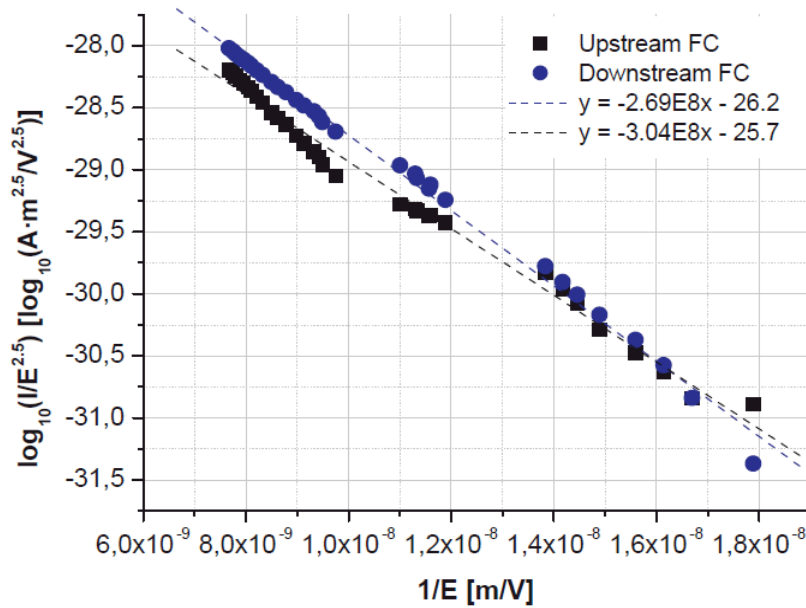


Fig. 7-3: Fowler-Nordheim plot of dark current.

#### 7.4 Dependence of dark current on RF pulse length

The SKIP pulse width cannot be varied by hundreds of nanoseconds. Hence, SKIP was switched off in order to evaluate the dependence of the dark current on the RF pulse width. The highest point was limited by the maximum voltage that can be applied to the klystron ( $E_S \approx 40$  kV). The dark current was measured for different pulse lengths (from 100 to 1600 ns) and different field values. The measured values reported in Fig. 7-4 show the linear dependence of the dark current on the RF pulse length.

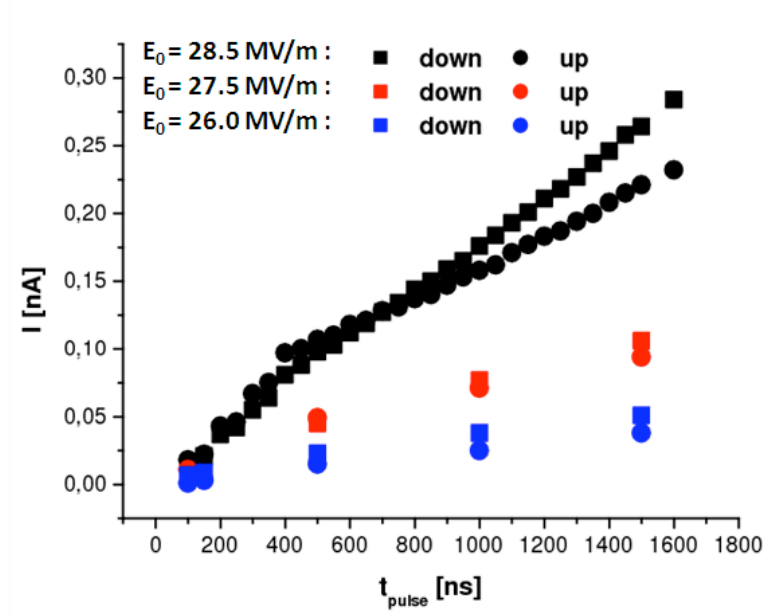


Fig. 7-4: Dependence of dark current on RF pulse length for different field values.

### 7.5 Breakdown rate measurements

The breakdown rate (BDR) is defined in the present paper by the breakdowns per pulse per meter (bpp/m) and is calculated as follows:

$$BDR = \frac{\text{Number of Breakdowns}}{t_{meas} \cdot PRF \cdot L_{struct}} \quad (\text{BD/pulse/m}),$$

where  $t_{meas}$  is the period of the measurement,  $PRF$  is the repetition rate, and  $L_{struct}$  is the length of the test structure (0.35 m).

### 7.6 Dependence of breakdown rate on accelerating gradient

The dependence of the breakdown rate on the accelerating gradient is presented in Fig. 7-5. Only data for which more than five breakdowns were counted and/or the measurement lasted more than 4 h were used in making this plot. The blue squares correspond to the BDR measurements performed during the structure conditioning and the red circles to those performed after the structure was conditioned. These points were measured with respect to the field value in the following order: 55.1, 52.7, 53.9, and 51.5 MV/m. As shown in the figure, the performance of the structure was significantly improved by conditioning.

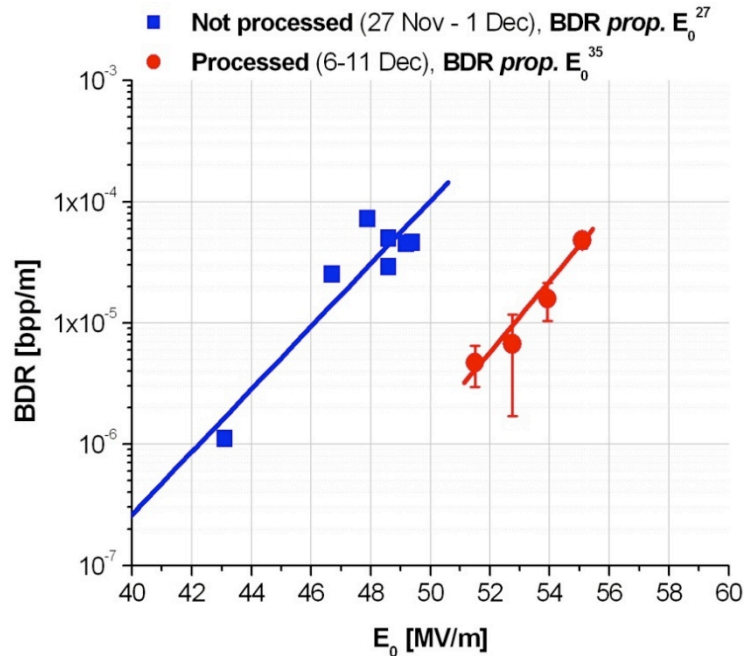


Fig. 7-5: Breakdown rate at different field values before and after conditioning.

Table 2 lists the main operating values (Operation) and electromagnetic quantities (EM quantities) of the four red points used to evaluate the dependence of the BDR on the accelerating gradient. If  $E_0$  is the accelerating gradient,  $E_{max}$  is the peak surface electric field, and  $P_{IN} \cdot freq/C$  is the input power multiplied by the frequency divided by the iris circumference, then the electromagnetic quantities  $E_0^{scaled}$ ,  $E_{max}^{scaled}$ , and  $(P_{IN} \cdot freq/C)^{scaled}$  are those scaled to a BDR of  $10^{-6}$  bpp/m by applying the scaling law  $E^3/BDR = \text{constant}$ . The quantity  $S_C^{scaled}$  is the maximum modified Poynting vector  $S_C$  scaled to a BDR of  $10^{-6}$  bpp/m by applying

the scaling law  $S_C^{15}/\text{BDR} = \text{constant}$ . These quantities are calculated according to the values listed in Table 2 and enable us to compare the present test structure with other structures in terms of performance.

For different accelerating structures, Figs. 7-6, 7-7, 7-8, and 7-9 respectively show the scaled values of the accelerating gradient, the surface electric field, the input power times frequency over iris circumference, and the modified Poynting vector. The black squares represent the X-band TW structures, the red diamonds represent the X-band SW structures, and the blue circles represent the 30-GHz TW structures. The horizontal lines represent the results for the present test structure.

Table 2: Main operating values and electromagnetic quantities used to evaluate dependence of BDR on accelerating gradient.

Magnitude	Point 1	Point 2	Point 3	Point 4	Unit
<i>Operation</i>					
$T_{rep}$	50	50	50	50	Hz
$t_{pulse}^{klystron}$	2.0	2.0	2.0	2.0	$\mu s$
SKIP status	on	on	on	on	-
$t_{pulse}^{SKIP}$	0.2	0.2	0.2	0.2	$\mu s$
$E_S^{klystron}$	35.5	34.5	35.0	34.1	kV
$P_F^{klystron}$	21.6	19.8	20.7	18.9	MW
$t_{operation}$	16	45	8	47.5	h
<i>EM quantities &amp; derived</i>					
$E_0$	55.1	52.7	53.9	51.5	MV/m
$E_{max}$	154	148	151	144	MV/m
$H_{max}$	176	169	173	165	kA/m
Pulsed Surf. Heating	2	2	2	2	degrees
$S_{C,max}$	2.4	2.2	2.3	2.1	MW/mm <sup>2</sup>
$P_{IN} \cdot freq/C$	14.0	12.9	13.4	12.3	MW · GHz/mm
<i>Breakdown Rate</i>					
No. breakdowns	48	19	8	14	-
BDR	$4.8 \cdot 10^{-5}$	$6.7 \cdot 10^{-6}$	$1.5 \cdot 10^{-5}$	$4.7 \cdot 10^{-6}$	bpp/m
<i>Scaled EM quantities</i>					
$E_0^{scaled}$	52.3	49.5	49.2	48.9	MV/m
$E_{max}^{scaled}$	136	139	138	137	MV/m
$S_{C,max}^{scaled}$	1.8	1.9	1.9	1.9	MW/mm <sup>2</sup>
$P_{IN} \cdot freq/C^{scaled}$	10.8	11.3	11.2	11.1	MW · GHz/mm

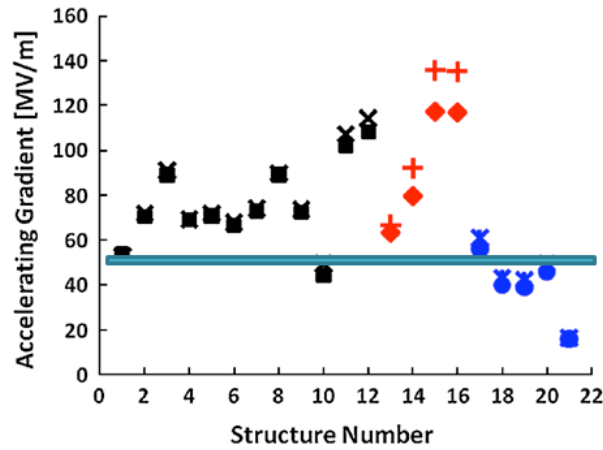


Fig. 7-6: Accelerating gradient for different high-gradient experiments as presented in [19]. The horizontal line is that from the present high-gradient test.

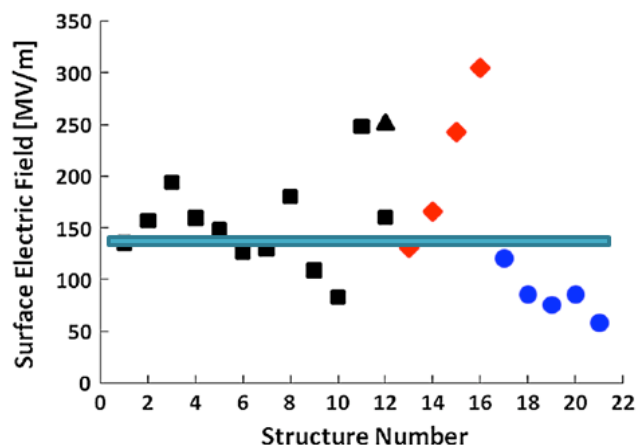


Fig. 7-7: Peak surface electric field for different high-gradient experiments as presented in [19]. The horizontal line is that from the present high-gradient test.

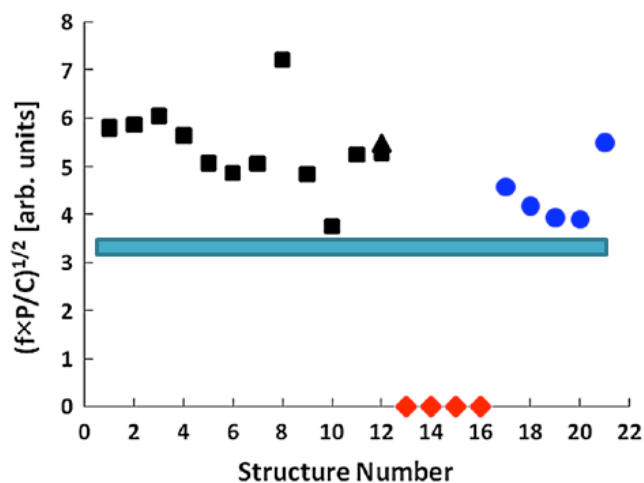


Fig. 7-8: Maximum  $P_{IN} \cdot freq/C$  for different high-gradient experiments as presented in [19]. The horizontal line is that from the present high-gradient test.

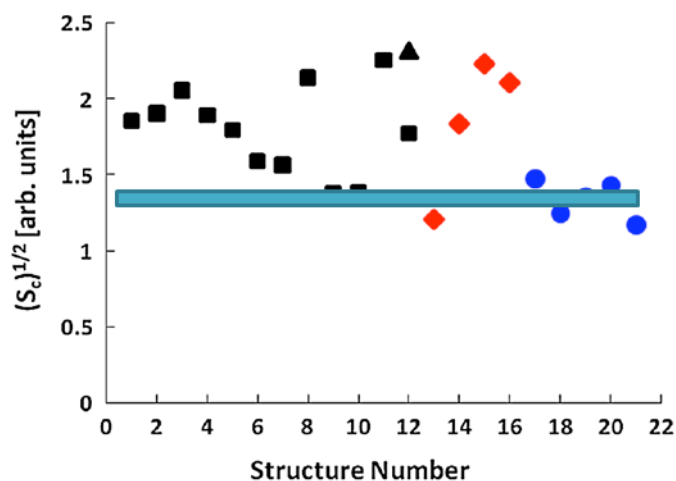


Fig. 7-9: Maximum modified Poynting vector  $S_c$  for different high-gradient experiments as presented in [19]. The horizontal line is that from the present high-gradient test.

## 7.7 Location of breakdowns along structure

### (a) Transmitted and reflected RF pulses

The distribution of breakdown events along a travelling-wave structure can be determined from the power drop suffered by transmitted pulses and the power increase in reflected pulses with every breakdown event (see Fig. 7-1). The breakdown location  $z$  is given by the following expression:

$$z = v_{group} (t_{Reflected} - t_{Transmitted} - t_{Delay}) / 2$$

where  $v_{group}$  is the group velocity of the structure,  $t_{Reflected}$  is the time within the RF pulse when the reflected power increases due to a breakdown start,  $t_{Transmitted}$  is the time within the RF pulse when the transmitted power drops due to a breakdown, and  $t_{Delay}$  is the time delay introduced by the length of the RF circuit between the structure input and the directional coupler that measures reflected pulses.

The distance between the structure input and the directional coupler for the present experimental setup is between 1.0 and 1.5 m, which introduces a round-trip time delay of about 10 ns in the detection of the reflected pulse. The filling time of the 22-cell structure is 50 ns. Therefore, in distance the time delay corresponds to 5 cells.

The RF pulses corresponding to the breakdown events registered from December 6 to December 12 were processed to determine the location at which each event took place. Figure 7-10 shows the breakdown distribution along the structure for the breakdowns registered from December 6 to December 12. Most of the breakdowns occurred towards the downstream end of the prototype, which indicates the existence of a hot region. It is to be noted that the accelerator column was cut, re-machined, structurally reinforced, and re-brazed to correct angular tilting of the output coupler with respect to the regular cell column. This repair may have created the hot region in question.

The results in the figure have an uncertainty in breakdown location of about 3 cells. The phase of the reflected RF pulse signal was not measured during this test, so a more precise location study of the breakdown events is not practicable.

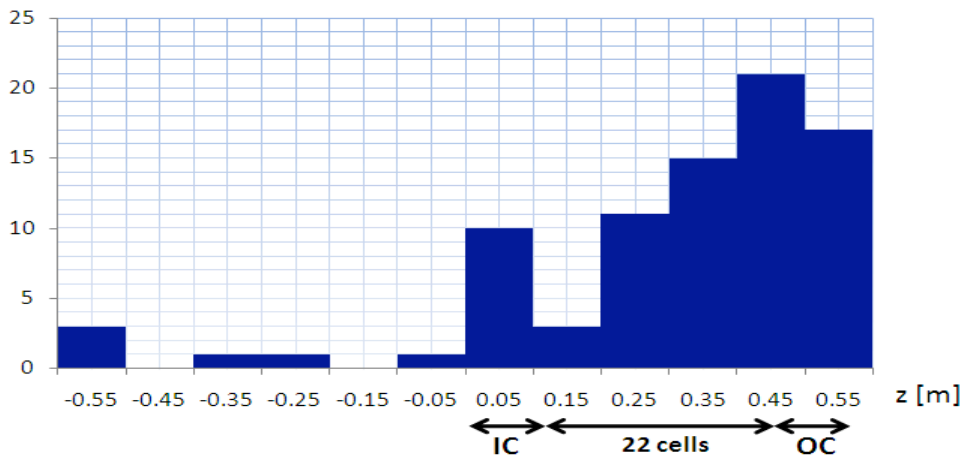


Fig. 7-10: Distribution of breakdowns along structure as obtained from study of RF pulses. the histogram shows accumulated breakdown events in a cell column, at the input coupler (IC), and at the output coupler (OC). The breakdown location has an uncertainty of about 3 cells ( $\sim 0.05$  m).

(b) *From acoustic emissions*

Typical acoustic pulse shapes for the breakdown events are shown in Fig. 7-11.

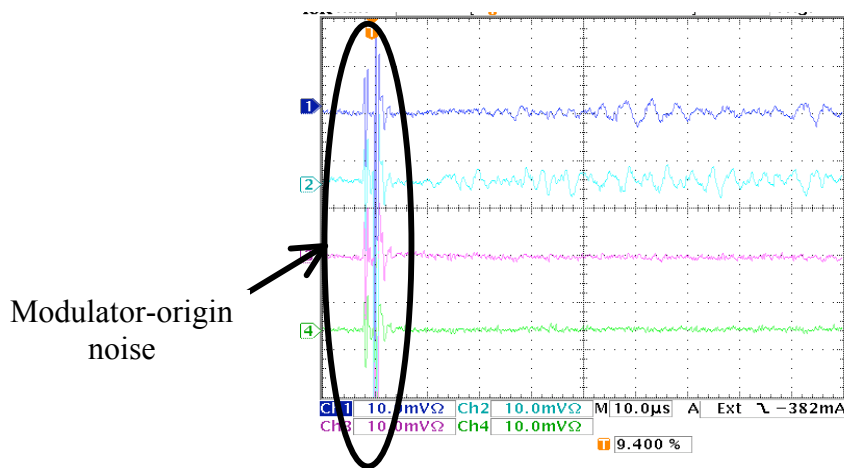


Fig. 7-11: Acoustic emission pulse shapes. Large initial spikes are due to the modulator-origin noise. The acoustic emission is measured a few microseconds after this noise.

The breakdown locations were also estimated from the appearance of large oscillation amplitudes in the acoustic signals monitored by the array of microphones shown in Fig. 5-7. The onset timing of this amplitude jump, which is related to the source location by the propagation of sound waves through the copper structure, was not utilized in this study. The result of the study is presented in Fig. 7-12. Two hot regions were found along the structure: one was in the upstream portion of the structure, and the other was at the downstream end. This seems inconsistent with the RF signal analysis shown in Fig. 7-10 and might have reflected the differences among the sensors with respect to sensitivity or mechanical contact. We think that further analysis taking into account such effects as well as the onset timing may give us a more consistent view, but this is beyond the scope of the present paper.

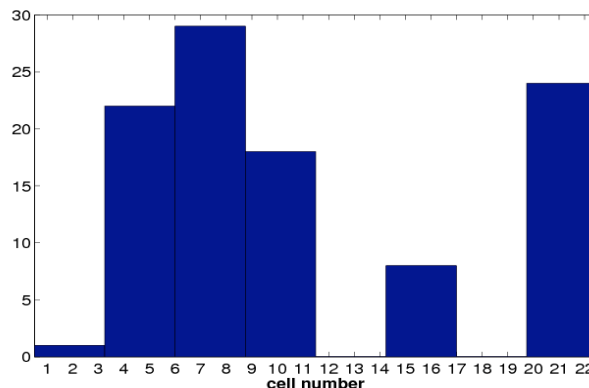


Fig. 7-12: Distribution of breakdowns along structure as estimated from acoustic signals.

An inspection of the interior surface will be decisive to know the most likely location for a breakdown to take place within the test structure. The structure will be cut at LNF to inspect the interior surface. If the inspection confirms the results of the present RF pulse study, then it will be reasonable to expect that better performance can be achieved with a structure that has not suffered any post-brazing repairs. This would mean that the accelerating structure for the energy upgrade of SPARC could operate at a much higher accelerating gradient than the prototype.

## 7.8 Missing energy when breakdown occurs

Some RF power is absorbed during breakdown. The absorbed energy, also known as missing energy, has been evaluated for several breakdown events of the C-band structure prototype. About 20% of the energy from the incident pulse is lost during breakdown.

## 7.9 Breakdown rate versus body temperature

The performance of the test structure at the working point ( $E_S = 35.5$  kV,  $P_F = 21.5$  MW) was studied for three different body cooling temperatures of 29.5°C (used for all previous measurements), 28.5°C, and 27.5°C, while the cooling water for the couplers was fixed at 30°C. Figure 7-13 shows the dependence of BDR on temperature. Each data point used for this study was measured over at least 12 h and represents at least 10 breakdowns.

During the measurement at 27.5°C the waveguides exhibited some activity, so the power was reduced in order to re-establish the normal operation of the whole structure. Then, the power was slowly increased from 22.8 kV to 35.5 kV, the working point of interest. The measurement of the BDR at 27.5°C was started just after 35.5 kV was reached. The BDR at 27.5°C was higher than that obtained for higher temperatures. It might be argued that the normal operation of the structure had not been completely re-established when the measurement at 27.5°C was started. However, on the basis of Fig. 7-13, we do not think that a change of a few degrees leads to a significant change in the BDR at this power level.

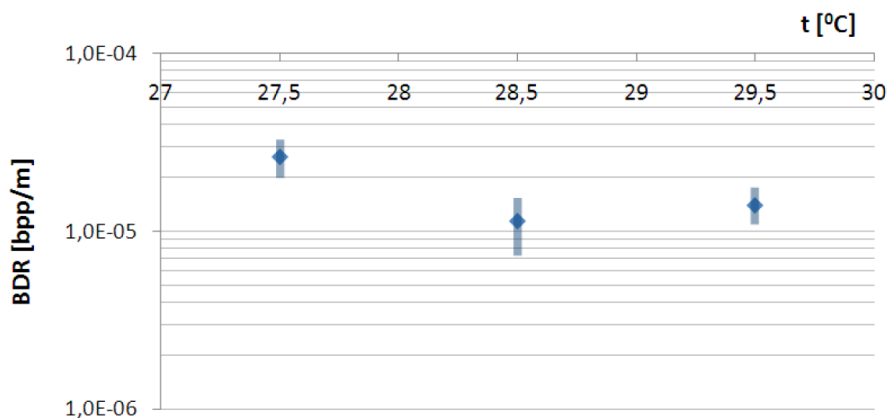


Fig. 7-13: Breakdown rate for different water temperatures used for body cooling.

## 8 DISCUSSION

### Conclusion of feasibility study on Frascati accelerator activities

The high-power tests of the C-band prototype carried out at KEK have confirmed the validity of the technical choices made by the LNF Accelerator Division. The good results obtained encourage us, INFN, to pursue without delay the realization of the longer accelerating sections that are necessary to increase the energy of the photoinjector SPARC. To this end, two 1.4-m constant-impedance units are currently in production. These will be entirely manufactured by local firms, including the final brazing as the LNF vacuum furnace is too small to contain them. The mechanical structure of the sections has been reinforced to reduce the risk of deformations during the delicate phase of high-temperature welding treatment. This should improve even more

the high field performance of the sections. The installation and operation of the complete C-band system in SPARC by late spring in 2012 is foreseen. In addition to reaching the important goal of increasing the beam energy, the installation of the C-band sections will allow studying the combined operation of two systems of different frequency in the same accelerator.

In Japan, the C-band system of the KEKB injector linac has been operated for many years with an accelerating field of 40 MV/m. Recently, the C-band linac of XFEL/Spring-8, consisting of 128 accelerator sections, was commissioned to operate at 35 MV/m on average after 1000 h of processing [20]. We had not encountered any opportunity to evaluate the high-gradient performance of the C-band accelerator structure at levels much higher than those. However, in the present experiment, a field level of greater than 50 MV/m was confirmed. This meant the possibility for us to apply the C-band accelerators to operate, as needed, with fields higher than the present operating level.

The results from the high-power test of the C-band structure prototype for SPARC constitute the first C-band data for research into the limitations on the high-gradient performance of accelerating structures. Until now, the collected data have shown that the maximum complex Poynting vector is a good measure for the high-gradient performance limits of accelerating structures working at the C-band, X-band, and 30 GHz.

The TERA Foundation performed a high-gradient test of a 3-GHz single-cell cavity at the CLIC Test Facility CTF3 at CERN (Switzerland) in 2010 [21]. The preliminary results of that test are also in agreement with the results obtained from other high-power tests. These preliminary results lie on the orange band in Fig. 8-1.

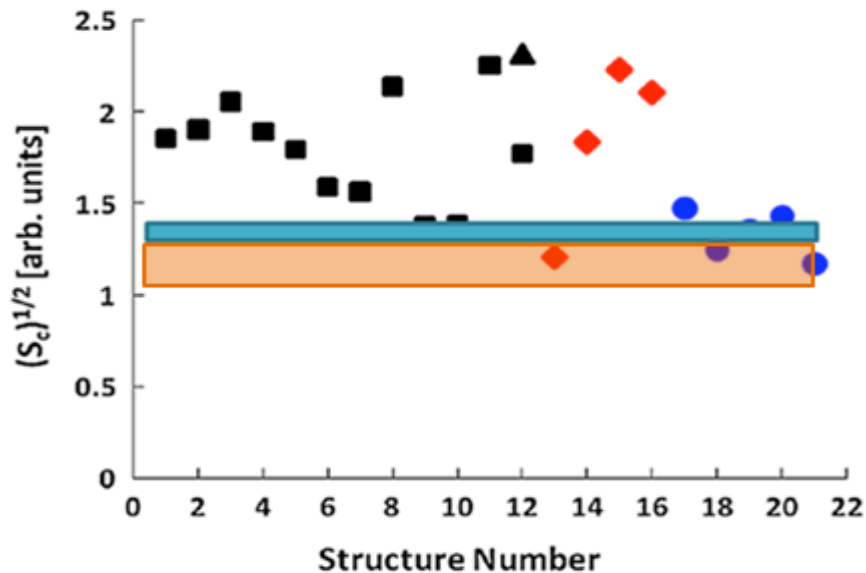


Fig. 8-1: Maximum square root of modified Poynting vector  $S_c$  for different high-gradient experiments as presented in [19]. The black squares represent the X-band travelling-wave structures, the red diamonds represent the X-band standing-wave structures, and the blue circles represent the 30-GHz travelling-wave structures. The orange band corresponds to the 3-GHz single-cell cavity tested by the TERA Foundation. The green band represents the present test of the C-band structure prototype for SPARC.

The results from the high-gradient test of the C-band structure prototype for SPARC are very encouraging for the studies that the TERA Foundation performs in the field of accelerators for hadron therapy. An accelerator for hadron therapy should not only deliver the appropriate beam and require little power but also be compact and reliable. Assuming that the modified Poynting vector is the quantity that limits the high-gradient performance of accelerating structures, and considering the modified Poynting vector of the C-band structure prototype for SPARC, an

accelerating field of 40 MV/m could be reached in a compact CABOTO-C (CARbon BOoster for Therapy in Oncology operating in the C-band) without compromising the machine reliability (BDR would be less than  $10^{-6}$  bpp/m, satisfying clinical requirements) [22].

## 9 ACKNOWLEDGMENTS

The authors warmly thank the Directors General of both laboratories, KEK and INFN Frascati, under the collaboration framework based on the MoU.

The authors thank the Operations Staff of Mitsubishi Electric Co. at the Electron-Positron Injector Linac of KEKB for their continuous operation of the test setup.

Special thanks are due to the Frascati technical staff, Mr. A. Battisti, Mr. R. Clementi, and Mr. S. Quaglia, for their valuable support during the test at KEK.

The contribution of S. Verdú-Andrés to the experiment at KEK was funded by the Seventh Framework Programme [FP7/2007-2013] under grant agreement No. 215840-2.

The research leading to these results has received funding from the European Commission under the FP7-INFRASTRUCTURES-2010-1/INFRA-2010-2.2.11 project TIARA (CNI-PP) grant agreement No. 261905.

## 10 REFERENCES

- [1] M. Ferrario et al., “Advanced Beam Dynamics Experiments with the SPARC High Brightness Photoinjector”, Proceedings of the IPAC2010 Conference, Kyoto, Japan, May 2010.
- [2] M. Ferrario et al., “Velocity Bunching Experiments at SPARC”, Proceedings of the 23rd PAC, Vancouver, Canada, May 2009.
- [3] T. Brabec, F. Krausz, “Intense Few-Cycle Laser Fields: Frontiers of nonlinear optics”, Rev. Mod. Phys. 72, 545-591 (2000).
- [4] V. Fusco, M. Ferrario, “Beam Dynamics Study of a C-band Linac Driven FEL with S-band Photoinjector”, Proceedings of the 23rd PAC, Vancouver, May 2009
- [5] S. Takeda, M. Akemoto, H. Hayano, H. Matsumoto, T. Naito, “High Gradient Experiments by the ATF”, PAC1991, San Francisco, CA, USA, 1991.
- [6] T. Kamitani, N. Delerue, M. Ikeda, K. Kakihara, S. Ohsawa, T. Oogoe, T. Sugimura, T. Takatomi, S. Yamaguchi, K. Yokoyama, Y. Hozumi, “Development of C-band Accelerating Section for SuperKEKB”, LINAC2004, Lübeck, Germany, 2004.
- [7] T. Higo, Y. Higashi, S. Matsumoto, K. Yokoyama, S. Doebert, A. Grudiev, G. Riddone, W. Wuensch, R. Zennaro, C. Adolphsen, V. Dolgashev, A. Jensen, L. Laurent, S.G. Tantawi, F. Wang, J.W. Wang, “Advances in X-band TW Accelerator Structures Operating in the 100 MV/m Regime”, IPAC10, Kyoto, Japan, 2010.
- [8] D. Alesini et al., “Design, Realization and Low Power RF Tests of the C band Structure Prototype for SPARC”, SPARC Note RF-11/002, 01/02/11, ([http://www.lnf.infn.it/acceleratori/sparc/TECHNOTES/RF/SPARC\\_RF\\_11\\_002.pdf](http://www.lnf.infn.it/acceleratori/sparc/TECHNOTES/RF/SPARC_RF_11_002.pdf)).
- [9] V.A. Dolgashev, “High Power Tests of Normal Conducting Single Cell Structures”, Proceedings of PAC07, Albuquerque, NM, USA, 2007.
- [10] [www.ansoft.com](http://www.ansoft.com)
- [11] C. Nantista, S. Tantawi, V. Dolgashev, “Low-Field Accelerator Structure Couplers and Design Techniques”, PRST-AB 7, 072001 (2004).
- [12] V.A. Dolgashev, “High Magnetic Fields in Couplers of X-Band Accelerating Structures”, Proceedings of the 2003 Particle Accelerator Conference, Portland, OR, USA, May 2003.
- [13] <http://www.comeb.it>

- [14] T. Sugimura, T. Kamitani, K. Yokoyama, K. Kakihara, M. Ikeda, S. Ohsawa, "SKIP - a Pulse Compressor for SuperKEKB", LINAC2004, Lübeck, Germany, 2004.
- [15] S. Verdú-Andrés, D. Alesini, R. Boni, G. Di Pirro, R. Di Raddo, M. Ferrario, A. Gallo, V. Lollo, F. Marcellini, L. Palumbo, B. Spataro, V. Spizzo, A. Enomoto, T. Higo, K. Kakihara, T. Kamitani, S. Matsumoto, T. Sugimura, K. Yokoyama, J. Kovermann, W. Wuensch, "The test of the C-band Structure Prototype for SPARC, an example of High Power RF test of High-Gradient Performance Accelerating Structures", Proceedings of the International Workshop on Multipactor, Corona and Passive Intermodulation MULCOPIM11, Valencia, Spain, 2011 (to be published).
- [16] H. Matsumoto and M. Ohtsuka, Proc. 24th Linear Acc. Meeting in Japan, Sapporo, July 1999, p.271 (in Japanese).
- [17] S. Ohsawa, T. Kamitani, T. Sugimura, K. Kakihara, M. Ikeda, T. Oogoe, S. Yamaguchi, K. Yokoyama, "Development of a C-Band Accelerating Module for SuperKEKB", LINAC2004, Lübeck, Germany, 2004.
- [18] J.W. Wang, G.A. Loew, "Field Emission and RF Breakdown in High-Gradient Room-Temperature Linac Structures", SLAC-PUB-7684, October 1997.
- [19] A. Grudiev, S. Calatroni, W. Wuensch, "New Local Field Quantity describing the High Gradient Limit of Accelerating Structures", Phys. Rev. Spec. Top. Accel. Beams 12, 102001 (2009).
- [20] K. Shirasawa et al., "Operation Status of the SACLA (Spring-8 Angstrom Compact free electron LASER) Main Accelerator", 5th Particle Accelerator Society of Japan, Tsukuba, Japan, August 2011 (in Japanese).
- [21] S. Verdú-Andrés, U. Amaldi, R. Bonomi, A. Degiovanni, M. Garlasché, A. Garonna, R. Wegner, C. Mellace, P. Pearce, "High-Gradient T of a 3 GHz Single-Cell Cavity", Proceedings of Linear Accelerator Conference LINAC2010, Tsukuba, Japan, 2010.
- [22] A. Degiovanni, S. Verdú-Andrés, "Expected High-Gradient Performances of Accelerating Structures for Hadrontherapy", TERA Internal Technical Note, Geneva, Switzerland, 2011 (in preparation).